Implications of Propeller-Wing Interactions on the Control of Aerodynamic-Surface-Free Tilt-Rotor Quad-Planes

Wechtler, N.; Mancinelli, A.; Smeur, E.J.J.

DOI
10.2514/6.2025-2129

Publication date
2025

Document Version
Final published version

Published in
Proceedings of the AIAA SCITECH 2025 Forum

AIAA SciTech Forum
6-10 January 2025, Orlando, FL
AIAA SCITECH 2025 Forum

10.2514/6.2025-2129

Implications of Propeller-Wing Interactions on the Control of Aerodynamic-Surface-Free Tilt-Rotor Quad-Planes

Noah Wechtler*, Alessandro Mancinelli† and Ewoud J.J. Smeur‡
Delft University of Technology, 2629HS Delft, The Netherlands

Quad-planes are a type of vehicle which combine the hovering capability of quadcopters and the forward flight efficiency of winged aircraft. Flight tests conducted on a dual-axis tilting-rotor quad-plane, designed to fly without aerodynamic surfaces, observed that the quad-plane suffered from insufficient roll authority during fast, forward flight. It was hypothesized that the propellers located in front of the wing are less efficient in generating a rolling moment due to potential propeller-wing interactions. Wind tunnel tests, performed at TU Delft's Open Jet Facility, confirmed a two- to fourfold reduction in roll moment generation from propellers mounted in front of the wing at similar levels of tilt as their rear counterparts. To address the mismatch in actuator effectiveness shown by the wind tunnel experiment, the effect of the propeller-wing interactions was incorporated into the aero-propulsive model of the quad-plane by means of a global polynomial, the structure of which was found using multivariate orthogonal function modelling. This augmented aero-propulsive model was then integrated into the sequential quadratic programming based control allocation algorithm used by the quad-plane. New flight tests demonstrated that, by including the propeller-wing interactions in the control allocation, the vehicle is capable of tracking a figure 8 maneuver without aerodynamic surfaces, and without compromising tracking performance.

I. Introduction

Quad-planes are a novel type of vehicle which combine the hovering capability of quad-copters and the forward flight efficiency of winged aircraft. Some quad-plane designs have separate rotors used for hovering and forward flight, such as the vehicle designed by Wang [1]. Other designs removed the need for separate hovering and forward flight propellers by incorporating tilting rotors. One such vehicle is the quad-plane developed by Mancinelli et al. shown in Figure 1. This particular quad-plane features four dual-axis tilt-rotors, which theoretically allow the vehicle to control all six degrees of freedom during hover, and five degrees of freedom during forward flight*. This offers new possibilities in the realm of disturbance rejection and dynamic maneuverability [2].

However, the dual-axis tilting rotors introduce additional complexity in terms of control system development and aero-propulsive modelling. The complexities in controlling the vehicle arise from the nonlinear actuator effectiveness. Mancinelli et al. proposed a Sequential Quadratic Programming (SQP) based algorithm which solves the Control Allocation (CA) problem by evaluating the nonlinear equations of motion. This CA algorithm is used in a modified Incremental Nonlinear Dynamic Inversion (INDI) control framework to effectively control the vehicle [3]. Particularly, INDI controllers are robust to model uncertainties [4] and external disturbances [5].

On the other hand, the aero-propulsive modelling of quad-planes has remained rather basic in comparison, with aerodynamic models often based on the classical small perturbation theory stability derivatives [2, 6]. In the case of the dual-axis tilt-rotor quad-plane this rudimentary approach has resulted in a major shortcoming. Namely, flight tests revealed that the quad-plane had insufficient roll authority during fast, forward flight. This was unexpected, as the drone should have full control over this degree of freedom.

To carry out a roll maneuver, the control system chooses a suitable input based on its knowledge of the system dynamics [3], which means that the aero-propulsive model must be able to predict the change in forces and moments that occur from a change in rotor tilt-angle. However, this change in propeller elevation does not only affect the force and moment production of the propellers through the introduction of a non-zero inflow angle, but it also affects the angle at which the wake of the propellers meets the wing, which in turn affects the wing aerodynamics. Evidently, the

*MSc. Student, Control and Simulation Department
†Ph.D. Candidate, Control and Simulation Department
‡Assistant Professor, Control and Simulation Department
*Due to gimbal lock, the propellers are unable to provide a lateral acceleration when the tilting mechanism is in forward flight configuration.

Figure 1 Dual-axis tilt-rotor quad-plane developed by Mancinelli et al. [2]. Photo courtesy of Nico Voß.

interactions between the different subsystems are quite complex and many of these effects are not yet taken into account during the control allocation on the vehicle. This provides an obvious avenue of improvement and possible solution for the lack of roll control in fast, forward flight.

Nevertheless, addition of these effects to the new aero-propulsive model cannot be too computationally complex as it is used in the INDI controller, which has to maintain a certain minimum control frequency to keep the system stable [7]. Furthermore, the drone can only carry a limited amount of computing hardware onboard, further limiting the set of feasible modelling techniques.

Due to the tilt-rotor nature of the vehicle, it is important to choose a propeller model which has the ability to predict propeller forces and moments when the propeller is operating at incidence. Theys et al. investigated how the propeller forces and torques vary as a function of the inflow angle [8]. They found that propeller thrust increases with the inflow angle. Rubin et al. attributed this to the fact that propellers act less like screws and more like rotating wings when the flow is parallel to the blades [9]. Additionally, Theys found that neither Blade Element Momentum Theory (BEMT) nor vortex lattice methods (VLM) accurately predicted the forces and torques across the entire range of inflow angles. Despite not accurately predicting forces and moments across the entire range of inflow angles, both methods did correctly identify the trends observed during the experiments. This sparked new developments such as the modified BEMT model by Leng et al. which uses an inflow correction to more accurately predict the forces at incidence [10]. Nevertheless, BEMT models currently require too much computational time to be used in real-time control. This was reinforced by the findings of Konuk and Landman, who tried to implement a modified BEMT model, but were unable to achieve sufficient computation speed for real time simulation [11], which is yet another step away from onboard control.

Therefore, despite potentially having lower accuracy, models using simple explicit equations appear to be the only viable option due to the real time computation constraint imposed by the control system. One such model was derived by Gill et al. [12]. They derived an analytical BEMT model, which uses simplifications to bypass the need of finding a solution to the force and torque equations iteratively [12]. Fernandez et al. recently compared various available modelling approaches for propellers operating at incidence, and concluded that the model derived by Gill provided accurate results and due to the low computational cost is quite suitable for real time control purposes [13]. In contrast, Simmons et al. used system identification and blending functions to identify a globally valid propulsion model [14]. The main differences between the method of Simmons and the other proposed models is that Simmons lets the model identify its own structure, whereas the other models are based on theoretical derivations. Using an approach similar to Simmons is also promising, as it results in a simple set of polynomial equations which satisfy the computational and continuity requirements imposed by the controller. However, the method of Simmons requires the determination of parameters through wind tunnel testing. Although the method derived by Gill et al. does not strictly require wind tunnel

data, using wind tunnel data to derive the model parameters leads to a more accurate model. This highlights a trend in the current propeller literature, namely that low order models require experimental data to produce accurate results throughout the entire range of inflow angles.

In contrast to propeller forces, the propeller-wing interactions of tilt-rotor vehicles are not as well documented, yet this phenomenon has also captured the attention of some researchers recently. For example, Yang et al. showed the slipstream curvature of a propeller at incidence from wind-tunnel experiments [15]. Additionally, they tried to model the slipstream using computational fluid dynamics (CFD), but CFD is far too computationally expensive to be used in real time simulation, let alone control. Meanwhile, most real time simulations use a momentum flow based method due to their simplicity and computational efficiency [16]. However, these methods assume that the flow behind the propeller is a cylinder without curvature, which is not applicable to the quad-plane as it neglects the fact that the freestream flow is not aligned with the cylinder and will therefore deform it. Conway derived an analytical solution from vortex theory, which can be used to determine the flow field behind a propeller [17]. This method of modelling propeller-wing interactions was recently applied to a tilt-wing tandem VTOL by May et al., but this method has not yet been experimentally validated for the particular application of tilt-rotor aircraft. Furthermore, the analytical vortex solution does not take into account wake curvature, so it remains unclear whether this method will provide accurate results when applied to a tilt-rotor configuration.

Lastly, Leng et al. describe a derivation based on vortex theory for an analytical model used to describe propeller-wing interactions, taking into account the effect of wing blockage on the wake [18]. Unfortunately, the analytical part of this model has not yet been extended to include the case of tilt-rotors. Clearly, there is a certain lack of propeller-wing interaction models tailored specifically around tilt-rotor vehicles, especially in the domain of real time computation.

Consequently, the goal of this research is twofold: First, investigate the lack of control over the roll axis during fast, forward flight by means of a wind tunnel campaign. Second, derive an extension to the stability derivative based aerodynamic model, with special emphasis on the propeller-wing interactions. With the additional constraint that the extension of the aerodynamic model must be compatible with the nonlinear CA algorithm and INDI controller used on the quad-plane.

II. Method

A. Reference Frames and Equations of Motion

Consider the quad-plane and the earth, body and propeller reference frames as shown in Figure 2. All coordinate systems are right-handed, of which the definitions are the following:

- Earth reference frame:
  - Origin fixed to the surface of the Earth.
  - $\hat{x}_e$ positive in the direction of North.
  - $\hat{y}_e$ positive in the direction of East.
  - $\hat{z}_e$ positive towards the center of the Earth.
- Body reference frame:
  - Origin fixed to quad-plane Center of Gravity (C.G.)
  - $\hat{x}_b$ positive out of the nose of quad-plane.
  - $\hat{y}_b$ positive out of the right wing.
  - $\hat{z}_b$ positive below the quad-plane.
- Propeller reference frame:
  - Origin fixed to center of rotation of i^{th} propeller
  - $\hat{x}_p^i$ positive pointing out of the nose of the quad-plane in hovering configuration.
  - $\hat{y}_p^i$ positive pointing right in hovering configuration.
  - $\hat{z}_p^i$ aligned with the motor rotation axis, pointing in opposite direction of thrust.

Including the wind and control reference frames not shown in Figure 2:

- Wind reference frame:
  - Origin fixed to quad-plane C.G.
  - $\hat{x}_w$ positive in the direction of the velocity vector of the quad-plane relative to the air.
  - $\hat{y}_w$ perpendicular to $\hat{x}_w$ and $\hat{z}_w$ positive to the right.
  - $\hat{z}_w$ positive below the aircraft.
- Control reference frame:

– Origin fixed to quad-plane C.G.
– $\hat{x}_c$ positive out of the front of the quad-plane, running parallel with the surface of the Earth.
– $\hat{y}_c$ perpendicular to $\hat{x}_c$ and $\hat{z}_c$ positive to the right.
– $\hat{z}_c$ positive towards the center of Earth.

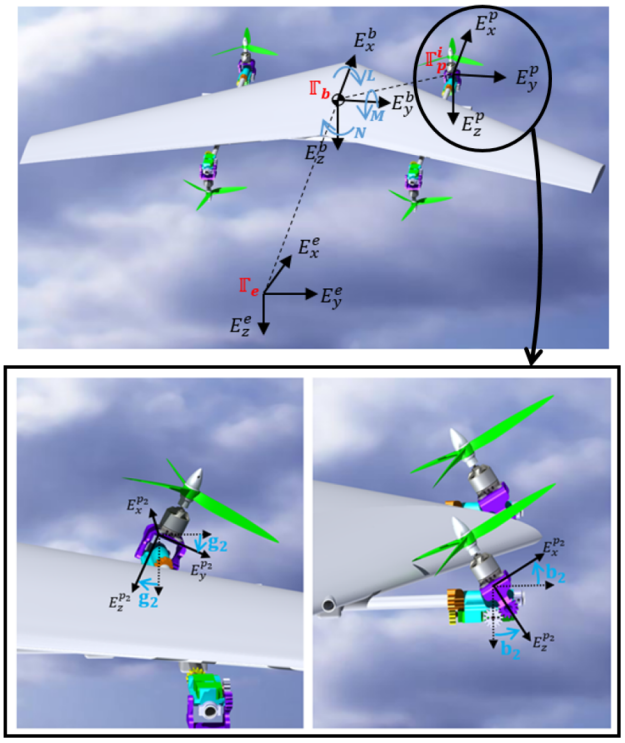

Figure 2 Quad-plane earth, body, and propeller frames [3]. Propeller elevation and azimuth are denoted by b_i and g_i respectively, starting with the first index in the front left and increasing clockwise. Note that the front left and rear right propellers spin counterclockwise, and the front right and rear left propellers spin clockwise.

The set of equations which govern the dynamics of the quad-plane can be expressed as:

where ${}^e\ddot{P}$ are the linear accelerations expressed in the Earth frame and ${}^b\dot{\omega}$ are the angular accelerations expressed in the body frame. m and I_b are the mass and moment of inertia of the vehicle, respectively. $\sum {}^e\boldsymbol{F}$ and $\sum {}^b\boldsymbol{M}$ are the sum of all forces and moments applied to the quad-plane, expressed in the earth and body frame, respectively. For simplicity, only the aerodynamic and propulsive forces and moments are considered:

$$\begin{cases} \sum {}^e\boldsymbol{F} = {}^e\boldsymbol{F}_p + {}^e\boldsymbol{F}_a \\ \sum {}^b\boldsymbol{M} = {}^b\boldsymbol{M}_a + {}^b\boldsymbol{M}_p, \end{cases} \tag{1}$$

where the subscripts a and p refer to aerodynamic and propulsive effects, respectively. Aerodynamic forces are often calculated in the wind reference frame to simplify the resulting expressions. To transform the aerodynamic forces to the desired earth reference frame, an intermediate rotation to the body frame is first taken:

$${}^bR_w = \begin{bmatrix} c_\alpha c_\beta & -c_\alpha s_\beta & -s_\alpha \\ s_\beta & c_\beta & 0 \\ s_\alpha c_\beta & -s_\alpha s_\beta & c_\alpha \end{bmatrix}, \tag{2}$$

where c and s are abbreviations of the sin and cos functions and α and β denote the angle of attack and angle of sideslip, respectively. Subsequently, the rotation from body to the earth reference frame can be achieved using:

$$
{}^{e}R_{b} = \begin{bmatrix} c_\theta c_\psi & -c_\phi s_\psi + s_\phi s_\theta c_\psi & s_\phi s_\psi + c_\phi s_\theta c_\psi \\ c_\theta s_\psi & c_\phi c_\psi + s_\phi s_\theta s_\psi & -s_\phi c_\psi + c_\phi s_\theta s_\psi \\ -s_\theta & s_\phi c_\theta & c_\phi c_\theta \end{bmatrix}, \tag{3}
$$

where θ is the pitch angle, ϕ the roll angle and ψ the yaw angle of the vehicle.

Similarly, the propulsive forces are usually calculated in the propeller reference frame. In this case, as the propellers are not fixed in alignment with the body, the forces and moments produced by the propellers are first converted to the body frame:

$$
{}^{b}R_{p}^{i} = \begin{bmatrix} c_{b^i} & 0 & s_{b^i} \\ s_{g^i} s_{b^i} & c_{g^i} & -s_{g^i} c_{b^i} \\ -c_{g^i} s_{b^i} & s_{g^i} & c_{g^i} c_{b^i} \end{bmatrix}, \tag{4}
$$

where b^i and g^i are the elevation and azimuth angle of the i$^{\text{th}}$ propeller respectively as denoted in Figure 2. The tilting mechanism's range of motion in elevation can be seen in Figure 3, with the tilt-angle in hover and forward flight denoted by b_{hover} and b_{flight}. Additionally, the mechanism can achieve a ±45 degree rotation side-to-side.

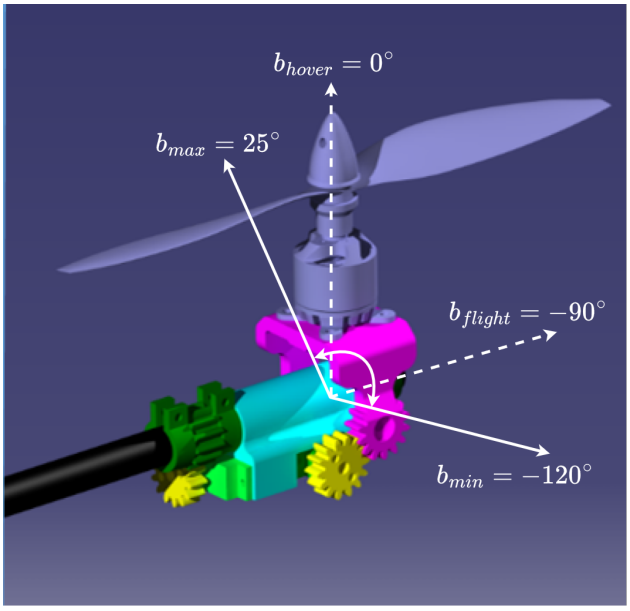

Figure 3 Elevation range of motion of the tilting mechanism, including hover and forward flight datums.

Lastly, the control allocation algorithm evaluates the linear accelerations in the control reference frame. The rotation from body to control reference frame is defined by:

$$
{}^{c}R_{b} = \begin{bmatrix} c_\theta & s_\phi s_\theta & c_\phi s_\theta \\ 0 & c_\phi & -s_\phi \\ -s_\theta & s_\phi c_\theta & c_\phi c_\theta \end{bmatrix}. \tag{5}
$$

B. Aerodynamic Model

As mentioned in the introduction, the aerodynamic forces are calculated using stability derivatives:

$$
{}^{e}\boldsymbol{F}_{a} = {}^{e}R_{b}\ {}^{b}R_{w} \frac{1}{2}\rho V^2 S \begin{bmatrix} C_{D_0} + k_{C_d}\left(C_{L_0} + C_{L_\alpha}\alpha\right)^2 \\ C_{Y_\beta}\beta \\ C_{L_0} + C_{L_\alpha}\alpha \end{bmatrix}. \tag{6}
$$

Where, in addition to the aerodynamic coefficients, the air density is given by ρ, the airspeed by V and the wing surface area by S.

Similarly, the aerodynamic moments expressed in the body frame are calculated using:

$$ {}^{b}\boldsymbol{M}_a = \frac{1}{2}\rho V^2 S \begin{bmatrix} b\left(C_{l_0} + C_{l_\beta}\beta + \frac{b}{2V}\left(C_{l_p}p + C_{l_r}r\right)\right) \\ c\left(C_{m_0} + C_{m_\alpha}\alpha\right) \\ \frac{b^2}{2V}\left(C_{n_p}p + C_{n_r}r\right) \end{bmatrix}, \tag{7} $$

where p, q and r are the roll, pitch and yaw rates. Additionally, the wingspan is represented by b and the mean aerodynamic chord by c.

None of the propeller-wing interaction models mentioned in the introduction generalized well to the tilt-rotor quad-plane, as they all neglect the case in which the rotors are able to tilt. This led to the adoption of a global error correction polynomial. This polynomial will be used to correct the dimensionless roll moment coefficient for the propeller-wing interactions. The reason behind using polynomials lies in the fact that they are simple to implement and troubleshoot, but any other approximation method could also be used.

For now, it is assumed that the roll moment correction is a function of the propeller rotational velocity Ω, the airspeed V and the propeller elevation angle b:

$$ \Delta C_{Mx} = f\left(\Omega_{1\text{-}4}, V, b_{1\text{-}4}\right), \tag{8} $$

which can be modelled by subtracting the roll moment coefficient generated by the wingless quad-plane from the roll moment coefficient generated by the regular quad-plane:

$$ \Delta C_{Mx}\left(\Omega_{1\text{-}4}, V, b_{1\text{-}4}\right) = C_{Mx_{\text{wing}}} - C_{Mx_{\text{wingless}}}. \tag{9} $$

Finally, the error correction term can be added in straightforward fashion to Equation 7:

$$ {}^{b}\boldsymbol{M}_{a,\text{new}} = {}^{b}\boldsymbol{M}_a + \frac{1}{2}\rho V^2 S \begin{bmatrix} b\Delta C_{M_x} \\ 0 \\ 0 \end{bmatrix}. \tag{10} $$

This process can easily be generalized to the other moment components as outlined in section IV.

C. Propulsive Model

The 5-component propeller model derived by Gill et al. [12] was implemented to replace the static thrust model used previously. This model maps the propeller forces and moments to the propeller rotational speed Ω, airspeed V and inflow angle i_p by assuming a specific blade geometry and treating the aerodynamics of the propeller blades as linear.

The aerodynamic properties of the propeller airfoil are described by c_{l_0}, c_{l_a}, c_{d_0}, c_{d_a}, c_{m_0} and c_{m_a}. δ represents the fraction of the propeller blade which is not useful, θ_{tip} is the propeller pitch angle at the tip and c_{tip} is the propeller tip chord.

First, the propeller radius R, rotational speed of the propeller, airspeed, and inflow angle are related to the climb ratio λ_c and advance ratio μ:

$$ \lambda_c = \frac{V\cos\left(i_p\right)}{\Omega R} \tag{11} $$

$$ \mu = \frac{V\sin\left(i_p\right)}{\Omega R} \tag{12} $$

Additionally, the propeller model depends on the solidity ratio σ:

$$ \sigma = \frac{N_b c_{tip}}{\pi R}, \tag{13} $$

and the induced inflow λ_i:

$$\lambda_i(\lambda_c,\mu)=\frac{1}{8}\left(-4\lambda_c+c_{l,a}\sigma(\delta-1)+\left(16\lambda_c^2+8c_{l,a}(\delta-1)\lambda_c\sigma\right.\right.$$
$$\left.\left.+\frac{1}{\delta}(\delta-1)\sigma\left(-8c_{l,0}\delta(1+\delta)+c_{l,a}\left(c_{l,a}(\delta-1)\delta\sigma-8\left(2\delta+\mu^2\right)\theta_{tip}\right)\right)-8c_{l,0}\mu^2\sigma\ln(\delta)\right)^{\frac{1}{2}}\right), \tag{14}$$

which can be summed with the climb ratio λ_c to obtain the total inflow λ:

$$\lambda=\lambda_c+\lambda_i. \tag{15}$$

The propeller thrust and drag coefficients are then computed as functions of the total inflow, and advance ratio and the propeller blade parameters:

$$C_{FT}(\lambda,\mu)=\frac{\sigma}{2\delta}\left((1-\delta)\left(c_{l,0}\delta(1+\delta)-2c_{l,a}\delta\left(\lambda-\theta_{tip}\right)+c_{l,a}\mu^2\theta_{tip}\right)-c_{l,0}\delta\mu^2\ln(\delta)\right), \tag{16}$$

$$C_{FX}(\lambda,\mu)=\frac{\mu\sigma}{2\delta}\left((1-\delta)\left(2c_{d,0}\delta+\theta_{tip}\left(\left(c_{l,a}-2c_{d,a}\right)\lambda+2c_{d,a}\theta_{tip}\right)\right)-c_{l,0}\delta\lambda\ln(\delta)\right). \tag{17}$$

Similarly, the roll, pitch, and yaw moment coefficients are computed:

$$C_{MR}(\lambda,\mu)=\frac{1}{2}(1-\delta)\sigma\mu\left(c_{l,0}(\delta+1)-c_{l,a}\left(\delta-2\theta_{tip}\right)\right) \tag{18}$$

$$C_{MP}(\lambda,\mu)=\frac{c_{tip}}{2\delta R}\sigma\mu\left(c_{m,a}(\delta-1)\left(\delta-2\theta_{tip}\right)-2c_{m,0}\delta\ln(\delta)\right) \tag{19}$$

$$C_{MQ}(\lambda,\mu)=\frac{1}{6}(1-\delta)\sigma\left(2c_{d,0}\left(1+\delta+\delta^2\right)+3c_{l,0}(\delta+1)\lambda+6\left(c_{d,a}\left(\lambda-\theta_{tip}\right)-c_{l,a}\lambda\right)\left(\lambda-\theta_{tip}\right)\right.$$
$$\left.+\frac{3\mu^2\left(c_{d,0}\delta+c_{d,a}\theta_{tip}^2\right)}{\delta}\right) \tag{20}$$

The propeller forces and moments, as defined in Figure 4, are expressed as functions of the aforementioned force and moment coefficients:

$$\begin{bmatrix}F_T\\F_x\\M_Q\\M_R\\M_P\end{bmatrix}=\begin{bmatrix}C_{FT}(\lambda,\mu)\,\frac{1}{2}\rho R^2(\Omega R)^2\\C_{FX}(\lambda,\mu)\,\frac{1}{2}\rho R^2(\Omega R)^2\\C_{MQ}(\lambda,\mu)\,\frac{1}{2}\rho R^3(\Omega R)^2\\C_{MR}(\lambda,\mu)\,\frac{1}{2}\rho R^3(\Omega R)^2\\C_{MP}(\lambda,\mu)\,\frac{1}{2}\rho R^3(\Omega R)^2\end{bmatrix}. \tag{21}$$

The resulting equations are computationally efficient due to their explicit nature. Nevertheless, the model accuracy heavily relies upon a set of nine parameters:

$$\begin{bmatrix}c_{l_0} & c_{l_a} & c_{d_0} & c_{d_a} & c_{m_0} & c_{m_a} & \delta & \theta_{tip} & c_{tip}\end{bmatrix}.$$

Gill proposed two methods to estimate these parameters. The first method, which is considered more accurate, consists of fitting the parameters to wind tunnel data using nonlinear optimization. As this method requires dedicated wind tunnel time, it was instead decided to go with the second method.

The second method assumes certain values based on observations made by Gill et al. during the making of their paper, which reduces the optimization problem into two separate root finding problems. This root finding problem only requires the static thrust and moment coefficient of the propellers, which had already been determined during initial

developments of the drone. A root finding algorithm is then used to determine the two remaining parameters, consisting of c_{l_a} and c_{d_a}.

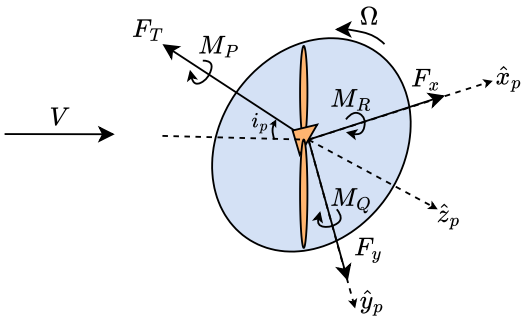

Figure 4 Counter-clockwise rotating propeller force and moment definitions [12]. For a clockwise rotating propeller, the direction of assumed positive M_Q and M_P are inverted.

The forces and moments computed by the propeller model are expressed in the propeller reference frame and need to be converted to the Earth reference frame:

$$ {}^{e}\boldsymbol{F}_p = \sum_{i=1}^{4} {}^{e}R_b^i \, {}^{b}R_p^i \begin{bmatrix} -{}^{p}F_x^i \\ 0 \\ -{}^{p}F_T^i \end{bmatrix}. \tag{22} $$

Likewise, the propeller moments expressed in the body frame can be computed:

$$ {}^{b}M_p = \sum_{i=1}^{4} \left(\begin{bmatrix} l_x^i \\ l_y^i \\ l_z^i \end{bmatrix} \times \left({}^{b}R_p^i F_p^i \right) + {}^{b}R_p^i \begin{bmatrix} (-1)^i M_R^i \\ M_P^i \\ (-1)^{i+1} M_Q^i \end{bmatrix} \right), \tag{23} $$

where l^i represents the distance between center of gravity and the i$^{\text{th}}$ propeller reference frame.

D. Computation of the Inflow Angle

As discussed in the previous section, part of the propeller model relies on the inflow angle i_p. The inflow angle is a function of propeller orientation and airspeed vector, and it can be determined using the definition of the angle between two vectors:

$$ \cos\left(i_p^i\right) = \frac{\boldsymbol{V} \cdot -{}^{b}\hat{\boldsymbol{z}}_p^i}{\|\boldsymbol{V}\| \left\| -{}^{b}\hat{\boldsymbol{z}}_p^i \right\|}, \tag{24} $$

$$ \sin\left(i_p^i\right) = \frac{\boldsymbol{V} \times -{}^{b}\hat{\boldsymbol{z}}_p^i}{\|\boldsymbol{V}\| \left\| -{}^{b}\hat{\boldsymbol{z}}_p^i \right\|} \cdot {}^{b}\hat{\boldsymbol{y}}_p^i. \tag{25} $$

Multiplying with ${}^{b}\hat{\boldsymbol{y}}_p^i$ in Equation 25 is necessary to distinguish between positive and negative elevation angles. Note that $\cos\left(i_p\right)$ and $\sin\left(i_p\right)$ are used directly by the propeller model, making it unnecessary to invert the expressions to obtain i_p itself.

However, these definitions are only valid for non-zero airspeed. Luckily, the outcome of the propeller model does not depend on the inflow angle when the airspeed is zero. Therefore, i_p can be assumed zero when the airspeed is zero. Alternatively, it is possible to leverage certain implementations of the arctan2 function to bypass the need for special treatment when the airspeed is zero. The definition of the inflow angle then becomes:

$$ i_p^i = \text{arctan2}\left(\left(\boldsymbol{V} \times -{}^{b}\hat{\boldsymbol{z}}_p^i \right) \cdot {}^{b}\hat{\boldsymbol{y}}_p^i, \boldsymbol{V} \cdot -{}^{b}\hat{\boldsymbol{z}}_p^i \right). \tag{26} $$

The sideslip angle can be discarded in the calculation of the inflow angle to further simplify the equations used in the real time control allocation:

$$i_p^i = b^i + \frac{\pi}{2} + \alpha, \tag{27}$$

where the $\frac{\pi}{2}$ offset is necessary, as the elevation angle and inflow angle are offset by 90 degrees due to the definition of b^i given in Figure 3.

E. Wind Tunnel Experiment

A wind tunnel test was carried out to identify the ΔC_{M_x} term used to model the roll moment generated due to propeller-wing interactions. This wind tunnel experiment was performed in TU Delft's Open Jet Facility.

The experiment contains four independent variables: airspeed, propeller rotational speed, front propeller elevation and rear propeller elevation. To reduce the number of test cases, and because the vehicle is symmetric, only the right side rotors were tilted. Additionally, propellers were all spun at the same RPM during each of the test cases. Furthermore, the setup was fixed at an angle of attack of six degrees, regardless of the velocity, as this is a representative angle of attack for the tested flight regime.

Figure 5 shows the test setup, including body and sensor reference frames.

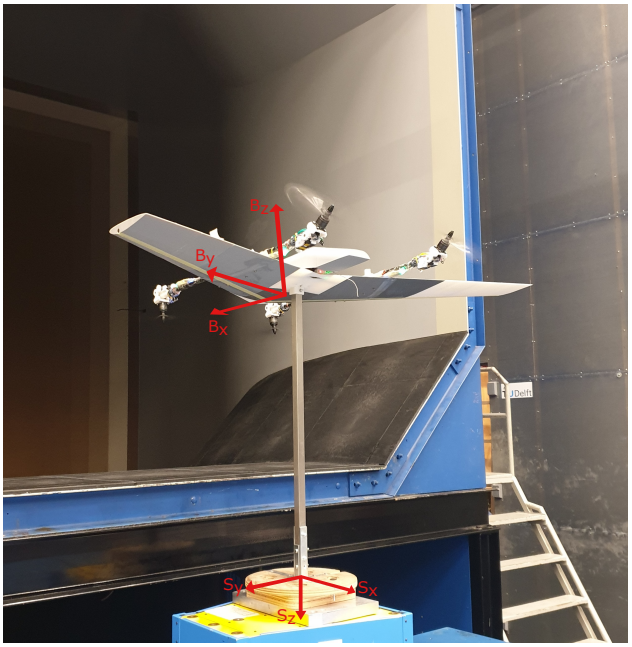

Figure 5 Wind tunnel experiment setup of the quad-plane, with sensor and body frames shown. Note that the drone is mounted upside down.

During testing, the wind tunnel velocity was varied between 9 and 15 meters per second in steps of three meters per second. The rotational velocity of the propellers was varied between 600 and 1000 radians per second. Cases in which the rotors could not produce more thrust than to overcome the drag caused by the quad-plane were discarded from the experiment to save time. The front and rear propellers were deflected from -120 to +20 degrees in increments of 10 degrees. Refer to Figure 2 and Figure 3 for a definition of these tilt angles. Unfortunately, the propeller elevation range had to be reduced to [-120, -60] degrees, when rotational velocities were equal to or exceeded 900 radians per second. This was done to limit the heat produced by the motors, as prolonged testing would eventually lead to a weakening of the Polylactic Acid (PLA) motor mount. An overview of the experiment matrix can be found in Table 1.

This experiment matrix was run twice, once with the complete drone and once without the wing, as shown in Figure 5 and Figure 6, respectively.

As mentioned previously, all propellers were spun at the same RPM. Consequently, it will not be possible to derive a model containing both front and rear propeller RPM as input. However, it is assumed that the front propellers dominate

Table 1 Range of propeller elevation angles tested during the wind tunnel experiment given certain wind tunnel and rotor speed combinations. Propeller elevation angles were varied in ten degree increments, and cases which were not tested are labelled N.T.

	600 [rad/s]	700 [rad/s]	800 [rad/s]	900 [rad/s]	1000 [rad/s]
9 [m/s]	[-120, 20]	[-120, 20]	[-120, 20]	[-120, -60]	[-120, -60]
12 [m/s]	N.T.	N.T.	[-120, 20]	[-120. -60]	[-120, -60]
15 [m/s]	N.T.	N.T.	N.T.	[-120, -60]	[-120. -60]

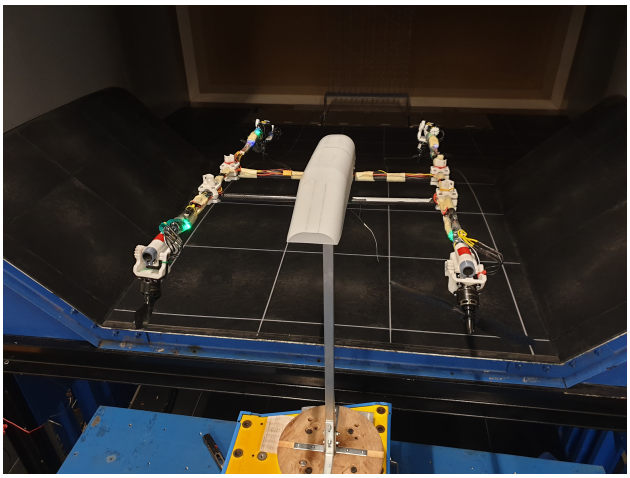

Figure 6 Wind tunnel experiment setup of the quad-plane skeleton.

the propeller-wing interactions, which is supported by subsection III.B. As such, it is unnecessary to include the RPM of the rear propeller in the derivation of the model. Additionally, only the right side propellers were tilted. Therefore, Equation 9 will be computed in two parts. First, the roll moment error coefficient as a function of right side propeller tilt (b_2, b_3) and front right propeller rotational speed (Ω_2) is computed:

$$\Delta C_{Mx_r}\left(\Omega_2, V, b_2, b_3\right) = C_{Mx_{\text{wing}}} - C_{Mx_{\text{wingless}}}. \tag{28}$$

Then, the roll moment error coefficient as function of left side propeller tilt (b_1, b_4) and front left propeller rotational speed (Ω_1) is computed using the same function and simply inverting the sign:

$$\Delta C_{Mx_l} = -\Delta C_{Mx_r}\left(\Omega_1, V, b_1, b_4\right). \tag{29}$$

Both terms can then be added to give rise to the final term used in Equation 9:

$$\Delta C_{Mx} = \Delta C_{Mx_r} + \Delta C_{Mx_l}. \tag{30}$$

F. Multivariate Orthogonal Function Modelling

To find suitable expressions for the error correction term ΔC_{Mx}, multivariate orthogonal function (MOF) modelling was employed. MOF modelling was chosen over regular polynomial fitting, due to MOF's ability to easily determine which terms are most relevant in modelling the response [19]. This is important due to the computational requirements imposed by the controller, to prevent overfitting, and to reduce the time spent searching for important terms. The QR-decomposition based method of generating orthogonal functions, described by Morelli et al. [20], will be outlined in this paper. Alternatively, the Gram-Schmidt procedure has also been used to generate orthogonal functions [19].

The first step is to settle on a set of suitable candidate modelling functions. Subsequently, the regular least squares problem is solved for all candidate modelling functions:

$$z = \boldsymbol{X}\boldsymbol{\Theta} + \epsilon, \tag{31}$$

where z is the N dimensional system response, $\boldsymbol{\Theta}$ the M dimensional vector of unknown parameters, $\boldsymbol{X}$ the $N \times M$ dimensional matrix of candidate modelling functions and $\boldsymbol{\epsilon}$ the N dimensional vector of equation errors.

The unknown parameter vector $\boldsymbol{\Theta}$ can be estimated by minimizing the least squares cost function:

$$J(\boldsymbol{\Theta}) = \frac{1}{2}(z - \boldsymbol{X\Theta})^T (z - \boldsymbol{X\Theta}), \tag{32}$$

which has the solution:

$$\hat{\boldsymbol{\Theta}} = \left(\boldsymbol{X}^T \boldsymbol{X}\right)^{-1} \boldsymbol{X} z^T. \tag{33}$$

Conventionally, the output of the regular least squares model is computed using:

$$\hat{\boldsymbol{y}} = \boldsymbol{X}\hat{\boldsymbol{\Theta}}. \tag{34}$$

However, the goal is to find a smaller subset of basis functions to model the error correction term. Therefore, the vector of modelling functions $\boldsymbol{X}$ can be orthogonalized using a QR decomposition:

$$\boldsymbol{X} = \boldsymbol{QR}, \tag{35}$$

where $\boldsymbol{Q}$ has the same dimensions as the matrix of modelling functions $\boldsymbol{X}$ and $\boldsymbol{R}$ is a square upper triangular matrix.

The general form of a MOF model is equal to that of the least squares model given in Equation 31. However, the matrix of modelling functions, $\boldsymbol{X}$, is now replaced with the orthonormal matrix $\boldsymbol{Q}$ obtained from QR decomposition:

$$z = \boldsymbol{Q}\boldsymbol{a} + \boldsymbol{\epsilon}, \tag{36}$$

where $\boldsymbol{a}$ is the unknown vector of orthogonal parameters.

The j$^{\text{th}}$ term of the unknown vector of orthogonal parameters, $\hat{a}_j$, is computed using the j$^{\text{th}}$ column of the orthonormal matrix $\boldsymbol{Q}$:

$$\hat{a}_j = \boldsymbol{q}_j^T z. \tag{37}$$

To determine which terms will be discarded, two metrics will be considered. First, the orthonormal modelling functions are chosen to minimize the Predicted Squared Error (PSE) [20]:

$$PSE = \frac{1}{N}\left(z^T z - \sum_{j=1}^{n}\left(\boldsymbol{q}_j^T z\right)^2\right) + \sigma_{max}^2 \frac{n}{N}, \tag{38}$$

where n is the number of considered candidate functions, and the maximum model fit error variance σ_{max}^2 can be estimated using [20]:

$$\sigma_{max}^2 = 25\hat{\sigma}^2 = 25\frac{(z - \hat{\boldsymbol{y}})^T (z - \hat{\boldsymbol{y}})}{N - n}. \tag{39}$$

The first term in Equation 38 is also referred to as the mean squared fit error (MSFE), whereas the second term is an overfit penalty, which is proportional to the number of chosen modelling functions. The PSE function has one global minimum, because the MSFE term decreases with each addition of a new function, whereas the overfit penalty increases with each addition of a new function [19]. The PSE criterion can further be reduced to:

$$\left(\boldsymbol{q}_j^T z\right)^2 > \sigma_{max}^2, \tag{40}$$

because $z^T z$, σ_{max}^2 and N solely depend on the dependent variable data [20].

Additionally, the orthogonal modelling functions are chosen such that they have a meaningful contribution to modelling the variation around the mean. This is done by computing the ΔR^2 achieved through addition of each new function. The ΔR^2 is computed using:

$$\Delta R_{min}^2 \leq \frac{\left(\boldsymbol{q}_j^T z\right)^2}{\left(z^T z - N\bar{z}\right)}, \tag{41}$$

where a ΔR^2_{min} cut-off of 0.005 was chosen [20].

Furthermore, due to the procedural nature of the orthogonalization algorithm, the order in which functions are introduced can greatly change the number of terms which are selected [21]. Since each orthogonal function depends on the previous function to form a basis, non-significant terms which appear before the final significant term must also be kept.

The least squares cost function for the orthogonal functions is given by:

$$J(\hat{\boldsymbol{a}}) = \frac{1}{2}\left(z^T z - \sum_{j=1}^{n}\left(\boldsymbol{q}_j^T z\right)^2\right), \tag{42}$$

where only $\left(\boldsymbol{q}_j^T z\right)^2$ is dependent on the chosen functions. Therefore, to reduce the dependence on the order of terms, terms should be sorted by their contribution to $\left(\boldsymbol{q}_j^T z\right)^2$ and they should be introduced in that order. All orthogonal functions which satisfy both the PSE and the ΔR^2 requirement are then chosen as the basis for the polynomial model. Finally, to obtain a physically meaningful polynomial, the ordinary least squares procedure is repeated, this time containing only the subset of m selected terms:

$$\hat{\boldsymbol{y}} = \boldsymbol{X}_m \hat{\boldsymbol{\Theta}}_m. \tag{43}$$

G. Controller Implementation of the New Aero-Propulsive Model

The quad-plane controller is based on an Incremental Nonlinear Dynamic Inversion (INDI) framework, wherein the nonlinear dynamic inversion is achieved through a Sequential Quadratic Programming (SQP) algorithm [3]. The cost function used in the nonlinear optimization is given by:

$$C(\boldsymbol{u}) = \|W_\nu\left(f(x,u) - \nu\right)\|^2 + \left\|\gamma^{\frac{1}{2}} W_u\left(u - u_d\right)\right\|^2, \tag{44}$$

where $f(x,u)$ are the nonlinear equations of motion of the vehicle expressed in the control reference frame, ν are the desired global accelerations, and u are the actuator inputs. The remaining terms are weights used to fine tune the solution.

As this scheme makes use of the nonlinear vehicle dynamics to find the solution to the CA problem, it is possible to integrate the derived aerodynamic model into the control allocation algorithm, provided that it does not increase the computational requirements beyond a certain threshold.

Upon implementing the new aero-propulsive model into the nonlinear controller, it was noticed that the CA algorithm prioritized tilting the rotors over increasing the angle of attack in some climb and straight flight conditions. Due to the model's dependence on airspeed and inflow angle, and the inclusion of the RPM in the cost function, the minimization of the cost function would result in a condition where the propellers were tilted excessively. The reason being that propellers generate larger forces at increasing inflow angles, given that RPM is kept constant. Therefore, the nonlinear program would converge to a solution which tilts the propellers to reduce the RPM. To solve this issue, the secondary objective term related to RPM was replaced by the motor power, as it is also a function of the inflow angle:

$$P^i_{motor} = M^i_Q\left(i^i_p, \Omega^i, V\right)\Omega^i, \tag{45}$$

where M_Q is the magnitude of the propeller yaw moment as given by Equation 20. The motor power was then normalized to keep the magnitude similar to other terms used in the optimization, effectively limiting the range to:

$$0 \leq P_s \leq 2. \tag{46}$$

The change in the secondary objective of Equation 44 is reflected by:

$$\left\|\gamma^{\frac{1}{2}} W_\Omega\left(\Omega - \Omega_d\right)\right\|^2 \rightarrow \left\|\gamma^{\frac{1}{2}} W_P\left(P_s - P_d\right)\right\|^2, \tag{47}$$

where W_P is a new weight related to the power.

III. Results

A. Polynomial Fit of Experimental Data

First, a set of basis functions was chosen, which were used to fit the wind tunnel data:

$$\begin{bmatrix} V_s & \Omega_{F,s} & \sin(b_F) & \cos(b_F) & \sin(b_R) & \cos(b_R) \end{bmatrix}, \tag{48}$$

where the subscripts F and R refer to the front and rear propellers respectively. The airspeed and propeller rotational velocity were scaled such that they stay within the range $[0, 2]$. Although there is no certain upper bound for the airspeed, it was assumed to be fifteen meters per second for this quad-plane. The rotational speed of the rotors are limited by the system to 1000 radians per second. The subscript s will be used whenever scaled values are used.

Then, both the data pertaining to the wing and wingless configuration were fit to a global fourth order polynomial. The full fourth order polynomial with six variables, including cross terms and a bias term, consists of 210 terms. However, the order of individual variables was limited to two to resolve issues with diverging polynomials, reducing the number of possible terms to 168. Table 2 shows the Root-Mean-Square Error (RMSE) of the polynomial fit, as well as the R^2 value. Additionally, the number of terms used in the MOF shortened polynomial are shown. Both shortened, and full polynomials show good agreement with the experiment data, with high R^2 values above 0.97 in all cases. Most importantly, the RMSE of the roll moment coefficient (C_{M_x}) is small, as the experiment was tailored around finding the influence of tilt on the roll moment.

Table 2 Comparison of the full and shortened fourth order polynomial fit of wing experimental data.

	RMSE full	R^2 full	RMSE short	R^2 short	n_{terms}
C_{M_x}	0.000939	0.998	0.00313	0.983	6
C_{M_y}	0.00876	0.999	0.0392	0.977	9
C_{M_z}	0.00118	0.997	0.00357	0.975	10

Similarly, the polynomials related to the wingless configuration show good agreement with the experimental data, with high R^2 values and low RMSE as shown in Table 3.

Table 3 Comparison of the full and shortened fourth order polynomial fit of skeleton experimental data.

	RMSE full	R^2 full	RMSE short	R^2 short	n_{terms}
C_{M_x}	0.000817	0.999	0.00317	0.989	6
C_{M_y}	0.00647	0.999	0.0391	0.974	10
C_{M_z}	0.00107	0.998	0.00453	0.972	10

Since the error term is a function of the wing and wingless polynomial, it is possible to obtain the coefficients exactly, as both polynomials can be subtracted from each other. This means that the resulting error terms have similar accuracy.

B. Roll Moment Investigation

The six terms which model the shortened roll moment coefficient polynomial for tilting the right side propellers are:

$$\begin{aligned} \Delta C_{Mx_r} = {} & c_1 \Omega_{2_s} \cos(b_2) + c_2 \Omega_{2_s} \sin(b_3) \cos(b_2)^2 + c_3 V_s^2 \Omega_{2_s} \cos(b_2) \\ & + c_4 \Omega_{2_s} \sin(b_2) \cos(b_3)^2 + c_5 \Omega_{2_s} \sin(b_3) \cos(b_3)^2 + c_6 \Omega_{2_s}^2 \cos(b_2), \end{aligned} \tag{49}$$

with the coefficients given in Table 4.

Table 4 Shortened roll moment coefficients for tilting right side propellers.

Coeff.	c_1	c_2	c_3	c_4	c_5	c_6
Value	0.012	-0.0040	-0.021	0.0045	-0.0065	0.0075

Note that there was no sensitivity analysis carried out with respect to choosing suitable PSE and ΔR^2_{min} values.

The roll moment can be plotted as a function of airspeed, propeller rotational speed and propeller elevation angle. Figure 7 shows the experimental data in a slow flight condition of nine meters per second, where the propellers are spinning at 600 radians per second. Clearly, using the front propellers to generate a rolling moment is inefficient when the wing is mounted. On the other hand, the presence of the wing has a negligible effect on the roll moment generation of the rear propellers.

The same holds true if the propeller rotational speed is increased to 1000 radians per second, as shown in Figure 8.

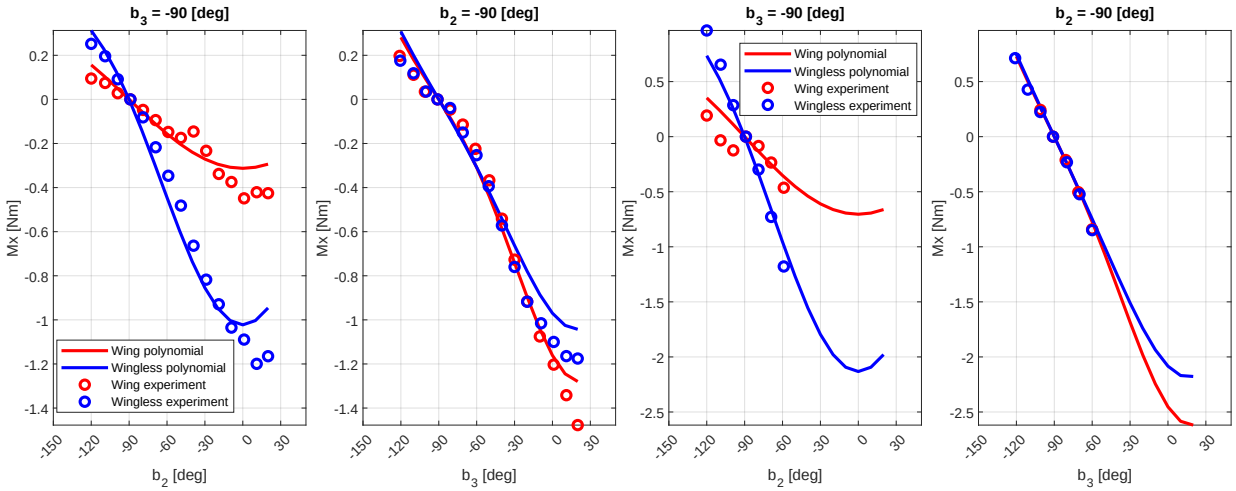

Figure 7 Rolling moment as a function of right side front (b_2) and rear (b_3) propeller elevation, Ω = 600 rad/s and V = 9 m/s. Zero degrees elevation corresponds to the hover configuration, and -90 to forward flight.

Figure 8 Rolling moment as a function of right side front (b_2) and rear (b_3) propeller elevation, Ω = 1000 rad/s and V = 9 m/s. Zero degrees elevation corresponds to the hover configuration, and -90 to forward flight.

The effect becomes slightly less pronounced at a higher airspeed of fifteen meters per second. Nevertheless, the rear propellers are still at least twice as effective in generating a roll moment as shown in Figure 9.

It is likely that the front propellers induce a downwash on the wing, which in turn reduces the lift produced by the wing section located behind the propellers. The local reduction in lift generates a roll moment which opposes the moment generated by front propellers, effectively reducing the total roll moment. This confirms the existence of non-negligible propeller-wing interactions, which result in an inaccurate estimation of the front rotor actuator effectiveness.

C. Determination of Propeller model parameters

As the propellers were not independently tested during the wind tunnel campaign, the propeller model parameters were obtained through the second method described by Gill et al. [12]. This method requires that the propeller was previously tested on a static test bed to determine the static thrust C_T and torque C_Q coefficients. Where the static propeller model is given by:

$$T = C_T\Omega^2, Q = C_Q\Omega^2. \tag{50}$$

The drone is using T-motor carbon fiber 10x5.5 propellers with a static thrust coefficient of $0.95 \cdot 10^{-5}[kg \cdot m]$ and a static moment coefficient of $1.31 \cdot 10^{-7}[kg \cdot m^2]$, obtained from static propeller testing. Additionally, the propeller tip chord was measured to be eleven millimeters, and the pitch at the propeller tip can be obtained using [12]:

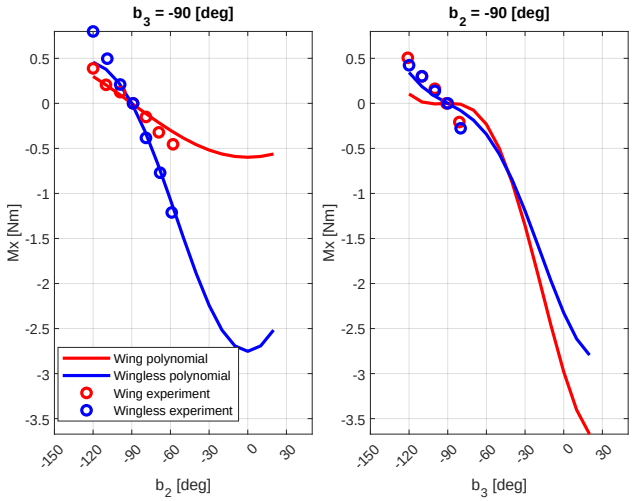

Figure 9 Rolling moment as a function of right side front (b_2) and rear (b_3) propeller elevation, Ω = 1000 rad/s and V = 15 m/s. Zero degrees elevation corresponds to the hover configuration, and -90 to forward flight.

$$\theta_{tip} = \frac{1.25P}{2\pi R}, \tag{51}$$

where P and R are the propeller pitch and radius, respectively. Furthermore, as there is no information present on the propeller airfoil, Gill recommends the usage of standard values for the following aerodynamic properties: the lift coefficient at zero angle of attack c_{l_0}, the moment coefficient at zero angle of attack c_{m_0} and the moment coefficient derivative with respect to alpha c_{m_a} should all be assumed equal to 0. The drag coefficient at zero angle of attack c_{d_0}, is set to 0.05. Finally, δ is assumed to be equal to 0.2. This reduces the problem to two separate root finding problems to determine the propeller c_{l_a} and c_{d_a}:

$$\text{find } c_{l_a} \text{s.t. } F_T\left(\Omega, V = 0, i_p = 0\right) = C_T\Omega^2, \tag{52}$$

$$\text{find } c_{d_a} \text{s.t. } M_Q\left(\Omega, V = 0, i_p = 0\right) = C_Q\Omega^2. \tag{53}$$

The parameters obtained through the static propeller model and root finding are shown in Table 5.

Table 5 Propeller model parameters obtained using static propeller thrust and moment coefficient.

C_{l_0}	C_{l_a}	C_{d_0}	C_{d_a}	C_{m_0}	C_{m_a}	δ	θ_{tip}	c_{tip}
0.0	3.42	0.05	0.32	0	0	0.2	0.22	0.011

D. Force-Torque comparison between Simulation and Wind tunnel Experiment

The aero-propulsive models including and excluding the roll moment correction were tested against the wind tunnel data, to ensure that adding the difference polynomials and propeller model had a positive effect on model accuracy. Table 6 shows the RMSE and error distributions of the new and old model in relation to the wind tunnel test data. Besides the vertical force, F_z, all forces and moments saw an improvement in the RMSE value. F_x saw an extreme improvement due to the new propeller model. Most importantly, the RMSE, mean and standard deviation of the error in M_x improved with the addition of the polynomials. It is expected that the roll behavior of the vehicle will improve due to the reduction of error in M_x.

Table 6 RMSE, and error distributions of the original model using pure stability derivatives and a static propeller model, and the new aero-propulsive model including ΔM_x and Gill's propeller model [12] with respect to wind tunnel data. μ is the mean error and σ is the standard deviation.

Case	ΔM_x and Gill prop			Pure stability derivs.		
	RMSE	μ	σ	RMSE	μ	σ
F_x [N]	2.6	0.80	2.4	10	9.6	4.3
F_z [N]	4.1	-3.4	2.3	3.3	-2.4	2.3
M_x [Nm]	0.31	-0.13	0.28	0.70	-0.31	0.63
M_y [Nm]	0.77	0.44	0.64	0.91	0.37	0.84
M_z [Nm]	0.36	-0.090	0.35	0.51	0.44	0.26

Similar to subsection III.B, further discussion of the simulation will be limited to the roll moment, as it is the primary focus of this study.

To show the effect of all the additions made to the aero-propulsive model, a comparison can be made between the wind tunnel data, the original aero-propulsive model which does not take into account ΔM_x, and the new aero-propulsive model which does takes into account ΔM_x. By taking the wind tunnel data as a ground truth, the accuracy of the models can be determined. Instead of directly using the wind tunnel data, the 168 term unshortened polynomial approximation described in subsection III.A was used as the ground truth to generate the contour plots in Figures 10-15. The rationale behind this decision was the need for perfectly spaced samples in the Matlab plotting functions.

Figure 10 shows the roll moment as a function of b_2 and b_3 at an airspeed of nine meters per second. Clearly, the inclusion of the error correction polynomial and the new propeller model resulted in a closer fit to the wind tunnel data. Additionally, the greater effectiveness of the rear rotors (b_3) in producing a roll moment is captured by the inclusion of ΔM_x.

Nonetheless, there are still has some considerable errors, as shown in Figure 11. The worst mismatch between wind tunnel data and the new model occurs when the inflow angle of the front and rear rotors are larger than ninety degrees. This is expected, as the propellers experience inflow from behind the propeller disk in this region, which likely has a highly nonlinear effect on their performance. Despite this shortcoming, there is still a much larger low error region compared to purely using stability derivatives.

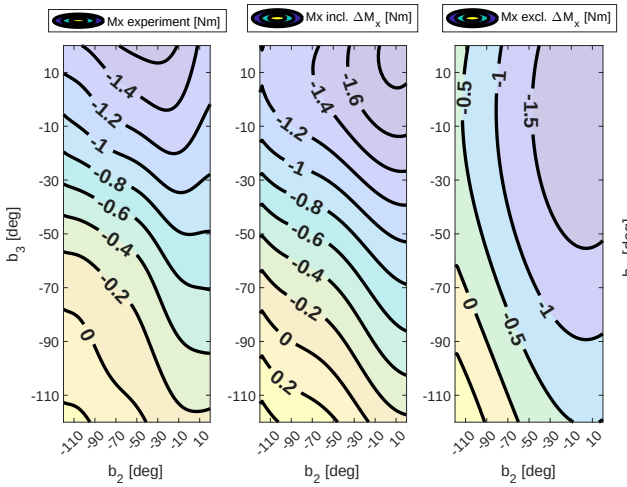

Figure 10 Comparison between experimental data, new aero-propulsive model and old model at V=9m/s and Ω = 600 rad/s.

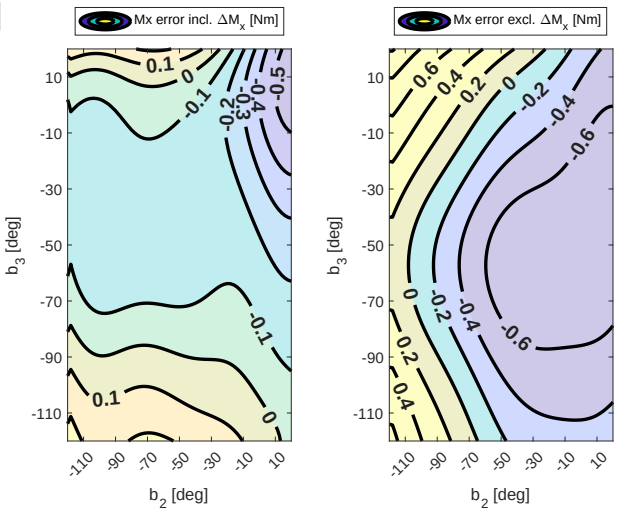

Figure 11 New and old aero-propulsive model error at V=9m/s and Ω = 600 rad/s.

Figure 12 shows the case in which the drone is flying at nine meters per second and the propellers are operating at maximum power. While the errors in the new model are still smaller than those of the original model, it is clear that even the model including ΔM_x fails to capture some nonlinearity exhibited by the experimental data. As the experiment data looks very predictable, it is possible that a polynomial which includes a few extra terms is capable of modelling this

region more accurately.

Once again, the regions of largest errors lie at the edges of the domain, as shown in Figure 13. Due to the limitations experienced during the wind tunnel test as mentioned in subsection II.E, only a small region of the total tilt mechanism envelope was covered for high RPM operations. Based on the experience with Figure 11, it is reasonable to assume that the error will only grow in the region beyond in which data was gathered. Therefore, it is likely that the difference polynomials misrepresent reality for high RPM and large elevation angles given the current data.

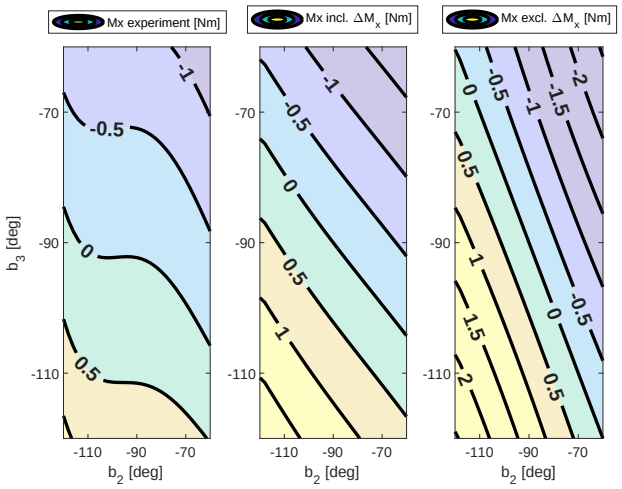

Figure 12 Comparison between experimental data, new aero-propulsive model and old model at V=9m/s and Ω = 1000 rad/s.

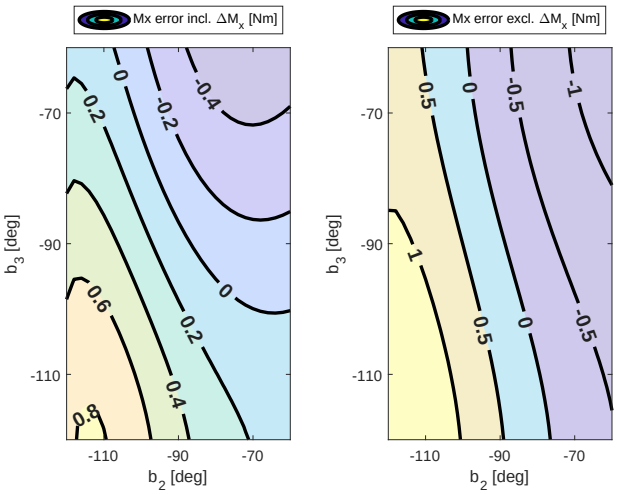

Figure 13 New and old aero-propulsive model error at V=9m/s and Ω = 1000 rad/s.

Figure 14 considers the case in which the drone is flying at fifteen meters per second and the motors are operating at 1000 radians per second. The outcome is similar as before, the model fails to capture some of the nonlinearity. However, compared to the previous case, the error grows much quicker in the direction of rear propeller elevation (b_3) as shown in Figure 15.

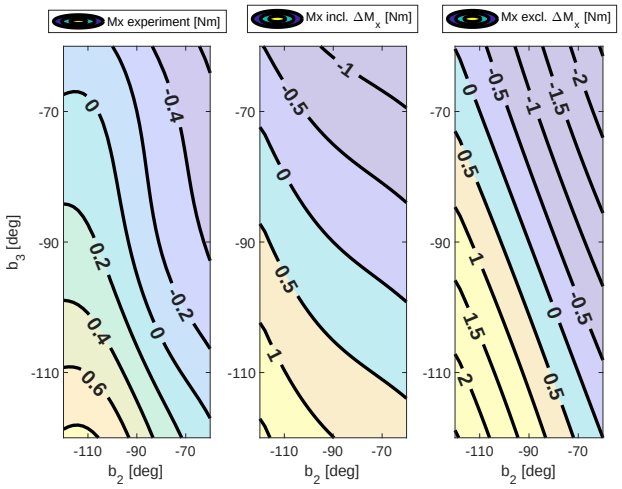

Figure 14 Comparison between experimental data, new aero-propulsive model and old model at V=15m/s and Ω = 1000 rad/s.

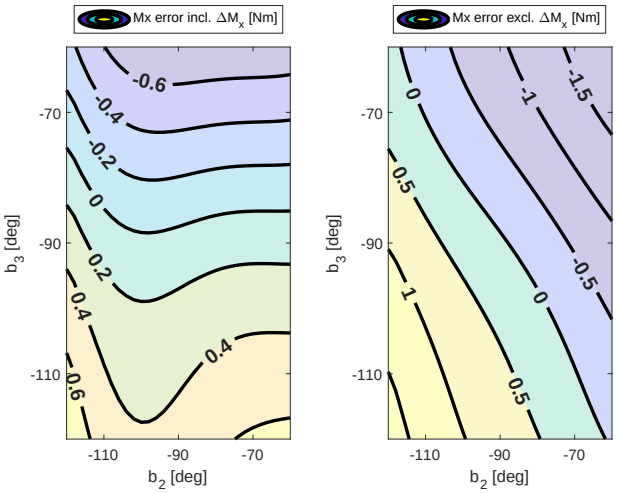

Figure 15 New and old aero-propulsive model error at V=15m/s and Ω = 1000 rad/s.

Overall, the global roll error correction polynomial reduces the difference between simulated and measured roll moments. Yet, in some cases the error remains substantial and due to the higher order nature of the polynomials the error might grow even faster outside the bounds in which wind tunnel testing was conducted.

E. Flight Test Analysis

The goal of the flight tests is to prove if the quad-plane can fly in common conditions without the use of aerodynamic surfaces. Three test flights were conducted. First a flight which included the roll moment correction polynomial and the propeller model developed by Gill et al. [12], however the drone was not allowed to use the ailerons. The second flight used the same controller, but the drone was allowed to use the ailerons. Finally, the same track was flown with the original model containing neither the error correction polynomials nor Gill's propeller model. The quad-plane was also allowed to use the ailerons during the last flight.

All flight tests followed the same circuit, consisting of four waypoints to form a lemniscate (also known as a figure 8 trajectory), as shown in Figure 19. Additionally, the drone had to track a constant airspeed of fifteen meters per second. The flight using the roll moment corrections without the ailerons shows some oscillations around the reference trajectory, mostly in the segment p1-p2. However, it should be noted that there was wind on the day of testing, reaching up to eight meters per second. The quad-plane experienced cross winds in segment p1-p2. An estimate of the forward component of the wind can be seen in Figure 16. Taking the wind into consideration, the quad-plane tracked the lemniscate adequately.

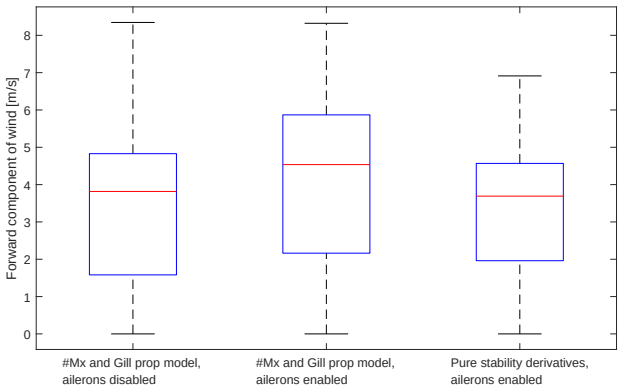

Figure 16 Absolute value of estimated wind speeds during each of the test flights.

1. Flight Path and Attitude Tracking

Through visual inspection of the flight path, it was already noted in the previous section that the flight not using ailerons showed some additional oscillations. To further compare the accuracy with which the drone tracks the circuit, a comparison between desired and actual XY-accelerations in the control reference frame can be made. Figure 17 shows very similar XY-acceleration tracking for all models using ailerons. However, when the drone is not using ailerons, a slight increase in lateral acceleration error is observed. This is visible at 4 and 16 seconds into the lemniscate trajectory, respectively. The flight in which no ailerons were used had the highest tracking error, as observed in Table 7.

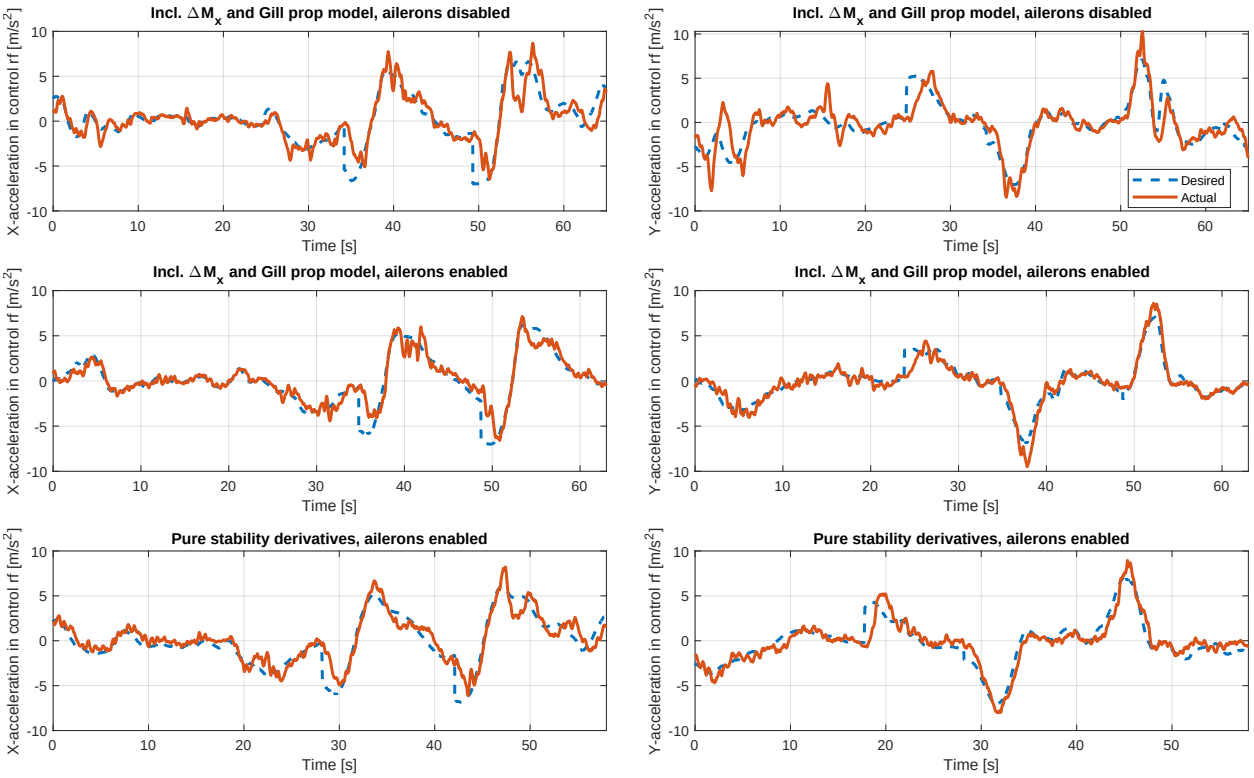

Figure 17 X- and Y-acceleration tracking of all models for one round of the lemniscate trajectory.

In addition to the linear acceleration, it is important to assess the attitude tracking of the drone with the model additions. Figure 18 shows the roll and pitch angle data collected throughout the flight tests. At a first glance, pitch angle tracking is similar between all models. This is further confirmed by the RMSE given in Table 7. More importantly, the worst roll angle tracking was observed in the case of no ailerons. This should be expected as the propellers are fully responsible for roll actions making them subject to saturation, whereas previously roll was fully delegated to the ailerons. The topic of actuator saturation will be further discussed in subsubsection III.E.2. Additionally, at 53 seconds, a sharp change in reference roll angle is observed. This happens as a result of experiencing a (near) negative angle of attack during a turn. This is an issue with the angle of attack estimation and should be investigated. If this artifact is removed, the RMSE across the flight test would decrease to 9.9 degrees, which would put it on par with the original model using ailerons. It should also be noted that the new model performed significantly better in tracking the roll angle when allowed to use ailerons, as shown in Table 7.

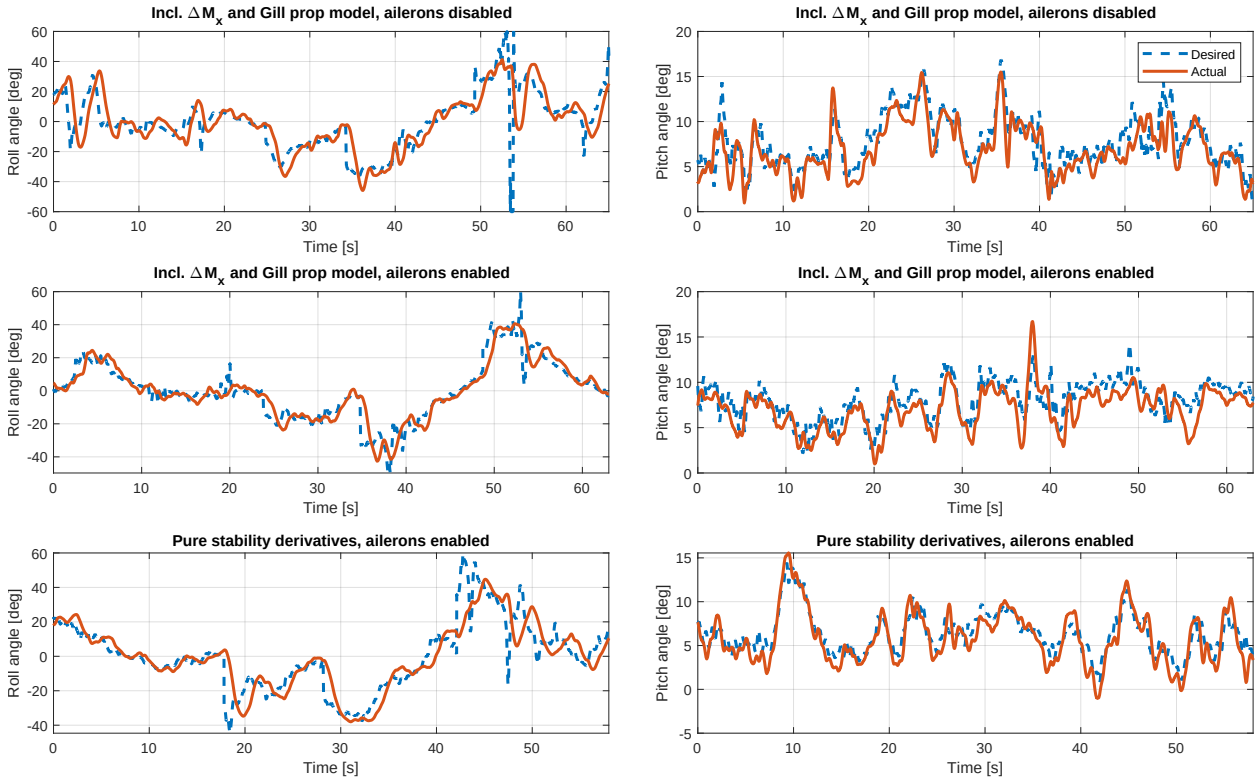

Figure 18 Roll and pitch angle tracking during lemniscate trajectory for all models.

On average, the quad-plane flew slower than the desired fifteen meters per second, regardless of the model used in control. The new model tracked airspeed slightly better, with a mean airspeed of 14.4 meters per second in both cases, and the original configuration with an average of 14.2 meters per second. Though, the RMSE are almost equal as shown in Table 7. The measured airspeed, wind speed and ground speed can be seen in Figure 20.

Table 7 Flight path and attitude tracking RMSE during lemniscate trajectory.

	Incl. ΔM_x ailerons disabled	**Incl. ΔM_x ailerons enabled**	**Original**
X-acc [m/s^2]	1.38	1.10	1.15
Y-acc [m/s^2]	1.44	0.75	0.96
θ [deg]	1.8	1.8	1.4
ϕ [deg]	12.7	6.5	10.3
V [m/s]	1.0	0.9	1.1

2. Actuator Commands

Intuitively, not using the ailerons requires more frequent deflections of the propellers, which can be seen in Figure 21. Compared to the other test flights, the propellers were deflected to a much higher degree, even leading to some saturation. This saturation is most noticeable at four seconds into the flight, and aligns with a worsening of the lateral acceleration tracking, as mentioned in the previous section.

Besides the short spike at 37 seconds, the elevation of the propellers remains much more limited in both cases where the quad-plane is allowed to use the ailerons. Additionally, the changes to the cost function mentioned in subsection II.G appear to lead to a more independent tilting of the rotors compared to the original.

No significant differences were observed in the desired motor speed commands given during the different flights, as shown in Figure 22. There are a few fluctuations in the commanded motor speed towards the end of the lemniscate

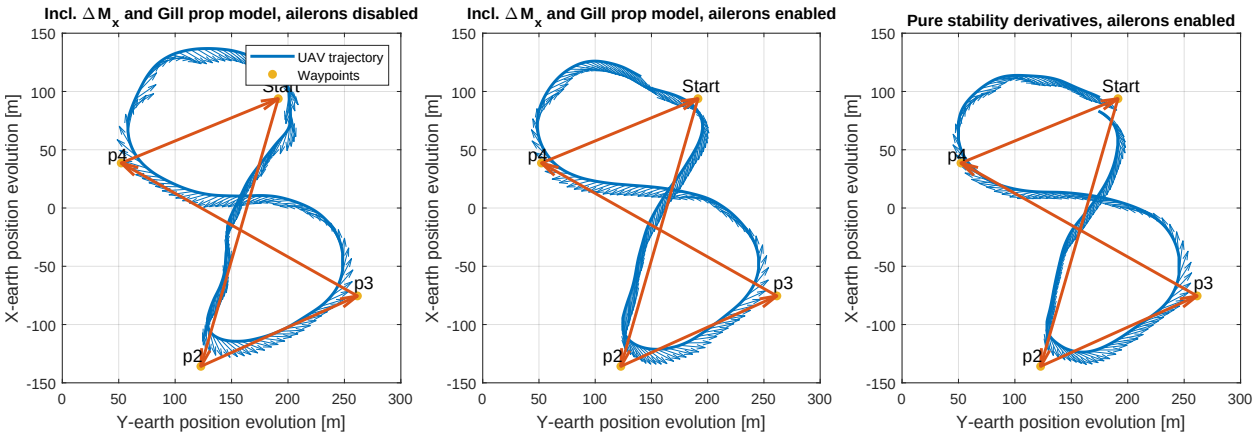

Figure 19 Flown path comparison of different models for one round of the lemniscate trajectory.

when the use of ailerons is prohibited, the reason of which is the issue with the angle of attack estimation mentioned in the previous section.

3. Impact on Computational Time

Finally, the impact of the error correction polynomials and more complex propeller model on the computational requirements of the control allocation algorithm can be assessed. To preface this discussion, it should be mentioned that the control allocation onboard the drone is performed in C, however the cost function is first derived in Matlab and subsequently converted to C code using the Matlab Coder[†] library. The process in which the cost function is derived was improved, resulting in fewer repeated computations in the new model. However, this optimization was not implemented for the original model, making a direct comparison unfair. The addition of equations to the model certainly contributes extra terms to the cost function, which means that in a fair environment, computation cost would also be increased.

In all cases the constraints imposed on the control allocation were equal, namely a time limit of 0.005 seconds, maximum number of cost function evaluations of 1000 and a maximum number of iterations of 200. Where an iteration occurs when the solver chooses a new point to evaluate. Table 8 gives an overview of the controller performance during the test flight. It is obvious that the time constraint is the dominant factor in terminating the optimization. Only in the case where no ailerons were used did the control allocation manage to have a slightly higher average frequency than the absolute minimum of 200 Hertz. It also had the largest amount of iterations and function evaluations. A more direct comparison can be made between the original model and the case in which the new model is allowed to use ailerons, as both are limited by the time constraint. On average, the original model achieved 6.0% more function evaluations. Although the new model computes slower than the original when ailerons are activated, the penalty in performance is not significant enough to hinder control of the quad-plane.

Table 8 Controller statistics

	Incl. ΔM_x ailerons disabled	**Incl. ΔM_x ailerons enabled**	**Original**
Mean freq. [Hz]	208	200	200
Mean func. evals	200	167	177
Mean iterations	95	79	88

[†]`https://mathworks.com/products/matlab-coder.html`

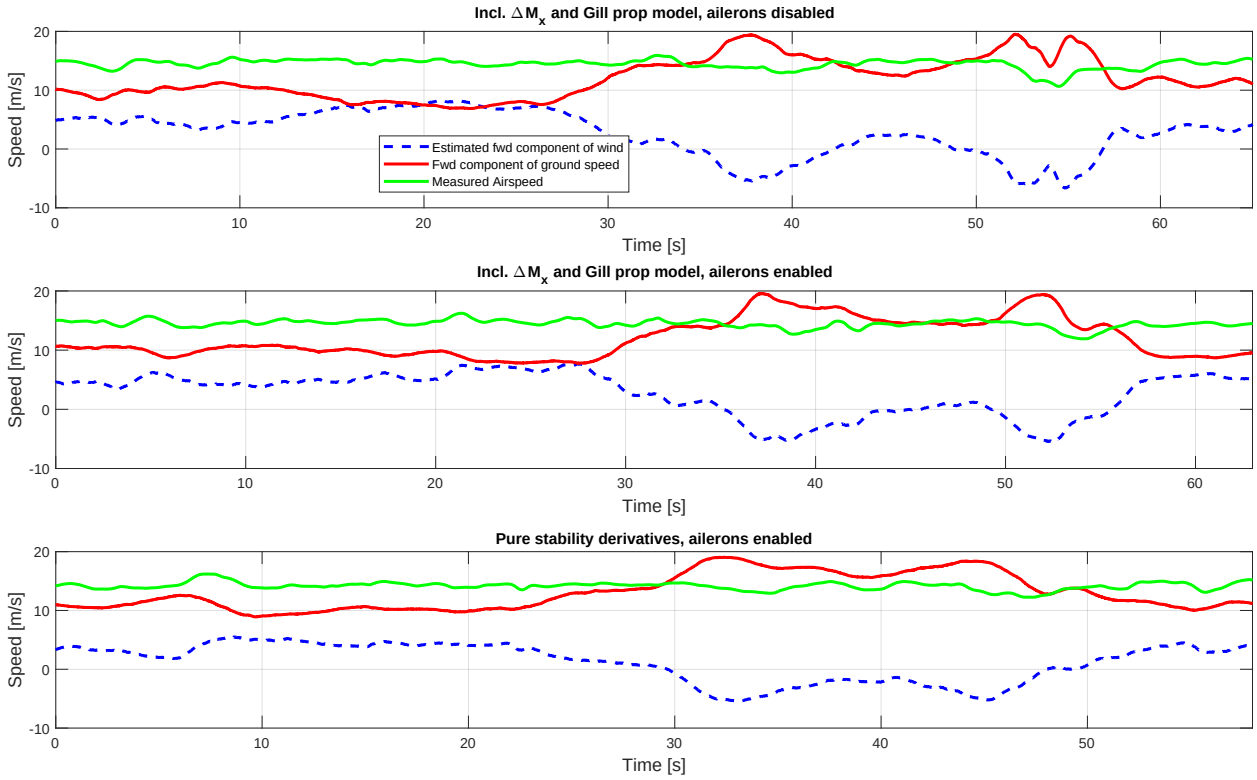

Figure 20 Airspeed tracking during lemniscate trajectory for all models.

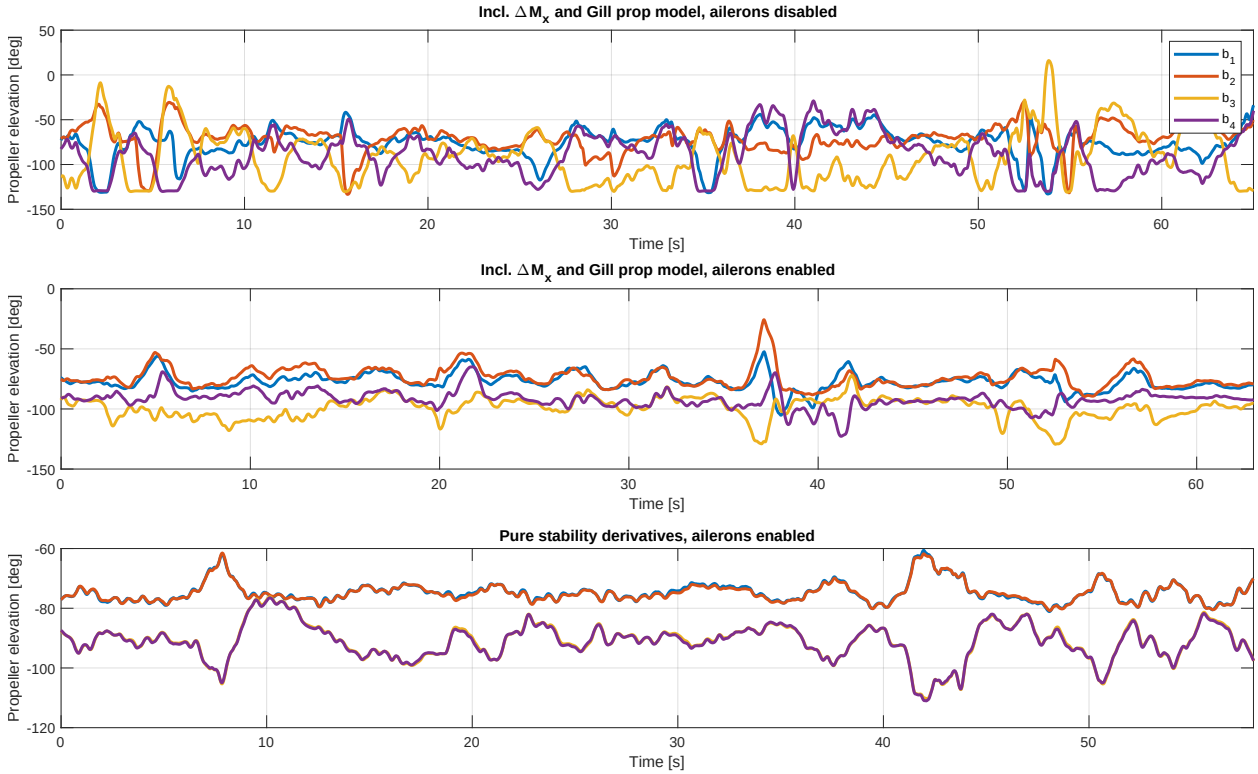

Figure 21 Propeller elevation states during lemniscate trajectory for all models. With b_1 being the front left propeller, b_2 the front right, b_3 the rear right and b_4 the rear left propeller.

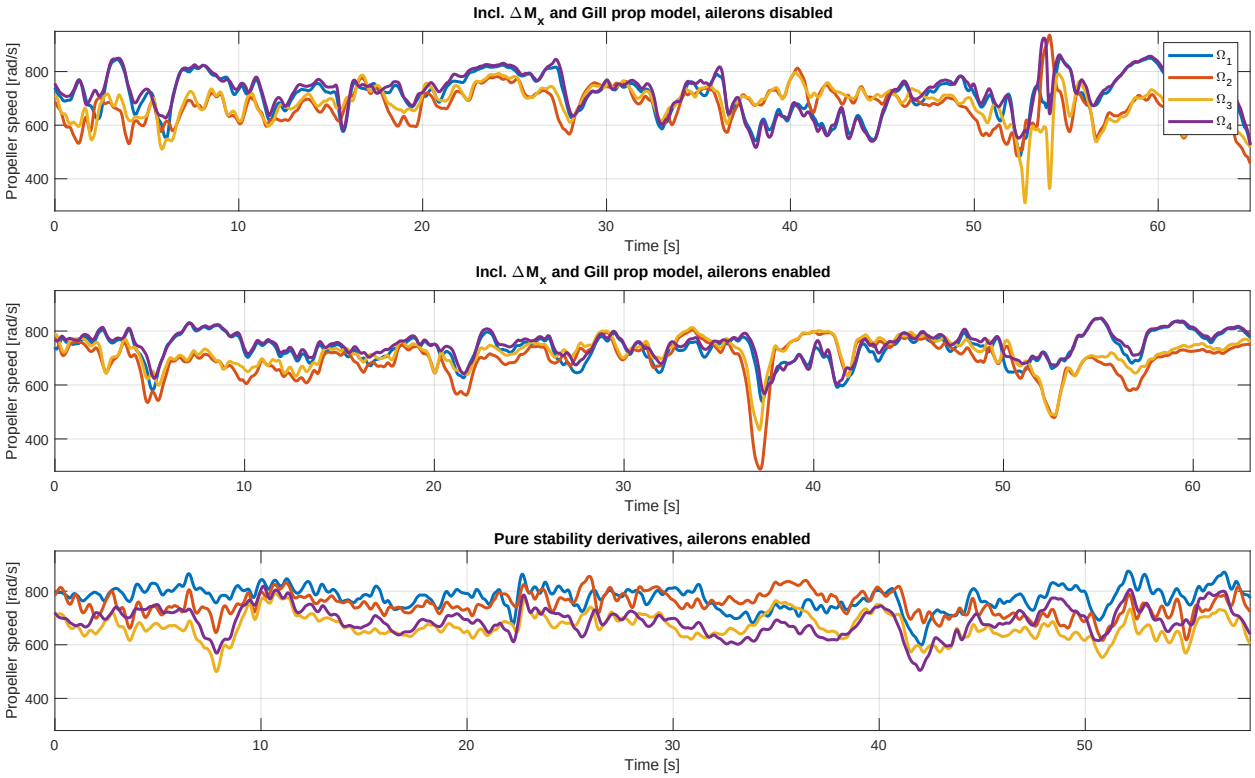

Figure 22 Motor speed states during lemniscate trajectory for all models.

IV. Conclusions

This paper highlights the importance of characterizing the propeller-wing interactions in vehicles using tilting rotors as the sole means of control. In the case of the dual-axis tilting rotor quad-plane designed by Mancinelli et al., wind tunnel testing showed that the propeller-wing interactions caused the front rotors to generate a two to four times weaker roll moment compared to an equal tilt of the rear rotors. The control allocation algorithm was not aware of this, preventing the drone from performing certain maneuvers in its aerodynamic-surface-free configuration.

By including the propeller-wing interactions in the new aero-propulsive model, the drone was able to track a figure 8 maneuver without ailerons. A small decrease in lateral acceleration and roll angle tracking accuracy was observed when compared to the flights using ailerons, but this decrease in accuracy was not significant enough to hinder operations. However, saturation of the tilt mechanism was observed, which could be a concern in certain circumstances, such as heavy gusts.

Propeller-wing interactions were approximated by a global polynomial obtained through multivariate orthogonal function (MOF) modelling. Although the global error-correction polynomials fulfilled their intended purpose of granting the drone the ability to fly without the use of ailerons, they still lack in accuracy due to their global nature. A sensitivity analysis with respect to Predicted Squared Error (PSE) and ΔR^2_{min} cut-off values could still be carried out to find a better trade-off between accuracy and number of polynomial terms. Lastly, it was difficult to obtain a set of polynomials which extrapolated well over the entire flight envelope and actuator space, as the wind tunnel experiment only covered flight between nine and fifteen meters per second.

Future research efforts could be directed at investigating the influence of the relative position between the wing and front rotors to minimize or even benefit from the effect of the propeller-wing interactions.

Appendix: Generalization of Error Correction Polynomials

Similarly to the roll moment coefficient, the pitch, and yaw correction coefficients can be expressed as functions of Ω, V and the propeller elevation:

$$\begin{bmatrix} \Delta C_{Mx} \\ \Delta C_{My} \\ \Delta C_{Mz} \end{bmatrix} = f\left(\Omega_{1\text{-}2}, V, b_{1\text{-}4}\right). \tag{54}$$

These coefficients are then related to the moment coefficients using the following expression:

$$\begin{bmatrix} \Delta M_x \\ \Delta M_y \\ \Delta M_z \end{bmatrix} = \begin{bmatrix} \frac{1}{2}\rho V^2 S b \Delta C_{Mx} \\ \frac{1}{2}\rho V^2 S c \Delta C_{My} \\ \frac{1}{2}\rho V^2 S b \Delta C_{Mz} \end{bmatrix}, \tag{55}$$

where c is the mean aerodynamic chord. The moment coefficients due to a tilt of the right hand side propellers are once again obtained by subtracting the moment measurements of the wingless quad-plane from the moment measurements of the full quad-plane:

$$\begin{bmatrix} \Delta C_{Mx}\left(\Omega_{1\text{-}4}, V, b_{1\text{-}4}\right) \\ \Delta C_{My}\left(\Omega_{1\text{-}4}, V, b_{1\text{-}4}\right) \\ \Delta C_{Mz}\left(\Omega_{1\text{-}4}, V, b_{1\text{-}4}\right) \end{bmatrix} = \begin{bmatrix} C_{Mx_{\text{wing}}} - C_{Mx_{\text{wingless}}} \\ C_{My_{\text{wing}}} - C_{My_{\text{wingless}}} \\ C_{Mz_{\text{wing}}} - C_{Mz_{\text{wingless}}} \end{bmatrix}, \tag{56}$$

which can be incorporated into the moment equations as follows:

$${}^{b}\boldsymbol{M}_{a,\text{new}} = {}^{b}\boldsymbol{M}_{a} + \frac{1}{2}\rho V^2 S \begin{bmatrix} b\Delta C_{M_x} \\ c\Delta C_{M_y} \\ b\Delta C_{M_z} \end{bmatrix}. \tag{57}$$

The pitch and yaw tracking was already sufficient prior to adding the error correction coefficients and including them would consume unnecessary computational resources, hence they were excluded from the controller. The pitch and yaw coefficients were however included in simulation, but did not significantly increase the accuracy of the model, as shown in Table 6.

References

[1] Wang, A., "Conceptual Design of a QuadPlane Hybrid Unmanned Aerial Vehicle," 2017. https://doi.org/10.13140/RG.2.2.23090.84163.

[2] Mancinelli, A., Smeur, E., Remes, B., and Croon, G., "Dual-axis tilting rotor quad-plane design, simulation, flight and performance comparison with a conventional quad-plane design," *2022 International Conference on Unmanned Aircraft Systems, ICUAS 2022*, Institute of Electrical and Electronics Engineers (IEEE), United States, 2022, pp. 197–206. https://doi.org/10.1109/ICUAS54217.2022.9836063.

[3] Mancinelli, A., Remes, B. D. W., De Croon, G. C. H. E., and Smeur, E. J. J., "Real-Time Nonlinear Control Allocation Framework for Vehicles with Highly Nonlinear Effectors Subject to Saturation," *Journal of Intelligent & Robotic Systems*, Vol. 108, 2023. https://doi.org/10.1007/s10846-023-01865-8.

[4] Sieberling, S., Chu, Q. P., and Mulder, J. A., "Robust Flight Control Using Incremental Nonlinear Dynamic Inversion and Angular Acceleration Prediction," *Journal of Guidance, Control, and Dynamics*, Vol. 33, No. 6, 2010, pp. 1732–1742. https://doi.org/10.2514/1.49978, URL https://doi.org/10.2514/1.49978.

[5] Smeur, E. J., de Croon, G. C., and Chu, Q., "Gust disturbance alleviation with Incremental Nonlinear Dynamic Inversion," *2016 IEEE/RSJ International Conference on Intelligent Robots and Systems (IROS)*, 2016, pp. 5626–5631. https://doi.org/10.1109/IROS.2016.7759827.

[6] Mimouni, M., Araar, O., Oudda, A., and Haddad, M., "A new control scheme for an aerodynamic-surface-free tilt-rotor convertible UAV," *The Aeronautical Journal*, 2023, p. 1–26. https://doi.org/10.1017/aer.2023.90.

[7] Nise, N. S., *Control Systems Engineering*, eighth ed., Wiley, Hoboken, NJ, 2019.

[8] Theys, B., Dimitriadis, G., Hendrick, P., and De Schutter, J., "Experimental and Numerical Study of Micro-Aerial-Vehicle Propeller Performance in Oblique Flow," *Journal of Aircraft*, Vol. 54, No. 3, 2017, pp. 1076–1084. https://doi.org/10.2514/1.C033618.

[9] Rubin, R. L., and Zhao, D., "New Development of Classical Actuator Disk Model for Propellers at Incidence," *AIAA Journal*, Vol. 59, No. 3, 2021, pp. 1040–1054. https://doi.org/10.2514/1.J059734.

[10] Leng, Y., Yoo, H., Jardin, T., Bronz, M., and Moschetta, J.-M., *Aerodynamic Modeling of Propeller Forces and Moments at High Angle of Incidence*, AIAA, 2019. https://doi.org/10.2514/6.2019-1332.

[11] Konuk, E., and Landman, D., *Computer Based Modeling for Tilt-Wing e-VTOL Propeller Performance*, AIAA, 2023. https://doi.org/10.2514/6.2023-0339.

[12] Gill, R., and D'Andrea, R., "Computationally Efficient Force and Moment Models for Propellers in UAV Forward Flight Applications," *Drones*, Vol. 3, No. 4, 2019. https://doi.org/10.3390/drones3040077.

[13] Fernandez, L. F., Bronz, M., Bartoli, N., and Lefebvre, T., *Assessment of Methods for Propeller Performance Calculation at High Incidence Angles*, AIAA, 2023. https://doi.org/10.2514/6.2023-2283.

[14] Simmons, B. M., "System Identification for Propellers at High Incidence Angles," *Journal of Aircraft*, Vol. 58, No. 6, 2021, pp. 1336–1350. https://doi.org/10.2514/1.C036329.

[15] Yang, H., Xia, W., Wang, K., and Hu, S., "Aerodynamic performance of a small-scale tilt rotor: Numerical simulation and experiment in steady state," *Proceedings of the Institution of Mechanical Engineers, Part C: Journal of Mechanical Engineering Science*, 2020. https://doi.org/10.1177/0954406220950352.

[16] Selig, M., *Modeling Propeller Aerodynamics and Slipstream Effects on Small UAVs in Realtime*, AIAA, 2010. https://doi.org/10.2514/6.2010-7938.

[17] Conway, J. T., "Analytical solutions for the actuator disk with variable radial distribution of load," *Journal of Fluid Mechanics*, Vol. 297, 1995, p. 327–355. https://doi.org/10.1017/S0022112095003120.

[18] Leng, Y., Bronz, M., Jardin, T., and Moschetta, J.-M., "Comparisons of Different Propeller Wake Models for a Propeller-Wing Combination," *8th European Conference for Aeronautics and Space Sciences*, Madrid, Spain, 2019. URL https://hal.science/hal-03385864.

[19] Morelli, E., *Efficient Global Aerodynamic Modeling from Flight Data*, AIAA, 2012. https://doi.org/10.2514/6.2012-1050.

[20] Morelli, E. A., *Real-Time Global Nonlinear Aerodynamic Modeling for Learn-To-Fly*, AIAA, 2016. https://doi.org/10.2514/6.2016-2010, URL https://arc.aiaa.org/doi/abs/10.2514/6.2016-2010.

[21] Morelli, E. A., "Practical aspects of real-time modeling for the learn-to-fly concept," *2018 Atmospheric Flight Mechanics Conference*, 2018, p. 3309.